OPEN ACCESS

GAVIN PUBLISHERS

Current Research in
Hydrology and Water Resources

Miadonye A et al. Curr Res Hydrol Res: CRHR-117.

DOI: 10.29011/CRHR-117. 100017

Review Article

Theoretical And Experimental Investigations of Optimum Conditions of Anthropogenic Carbondioxide Geological Storage in Saline Aquifers

Adango Miadonye[1*], Mumuni Amadu[2], Tochukwu G. Nwajiaku[2]

[1]Department of Chemistry, Cape Breton University, Sydney, NS, Canada

[2]Department of Process Engineering and Applied Science, Dalhousie University, Canada

[*]**Corresponding author:** Adango Miadonye, Department of Chemistry, Cape Breton University, Sydney, NS, Canada. Tel: +1-9023171422; Email: adango_miadonye@cbu.ca

Citation: Miadonye A, Amadu M, Nwajiaku TG (2018) Theoretical and Experimental Investigations of Optimum Conditions of Anthropogenic Carbondioxide Geological Storage in Saline Aquifers. Curr Res Hydrol Res: CRHR-117. DOI: 10.29011/CRHR-117. 100017

Received Date: 11 October, 2018; **Accepted Date:** 29 November, 2018; **Published Date:** 06 December, 2018

Abstract

With increasing concentration of anthropogenic carbon dioxide in the atmosphere and the attendant global warming, geological sequestration of this greenhouse gas has been accepted as a technically and economically mitigation option. In this regard, a targeted geological repository with a promising global storage potential is a saline aquifer. In these geologic systems, decreasing water wettability due to acidity evolution following carbon dioxide injection will be the primary cause for its increased relative permeability or relative mobility. This increased relative permeability will increase brine fractional flow in saline aquifers and, hence, cause efficient displacement and maximization of storage pore volumes.

Decreased wettability will be due to the dissociation of carbonic acid in formation brine and increased hydrogen ion concentration. This dissociation will depend on the dissociation constant of carbonic acid at aquifer temperature and salinity. Therefore, in trying to find optimum conditions of dissociation, the temperature dependence of the dissociation constant is of prime importance. In this paper, we have integrated theories of temperature dependent ionization of carbonic acid, interfacial tension dependence on intermolecular forces and fractional flow to propose hypotheses regarding optimum geological conditions for sequestration. Accordingly, we have tested these hypotheses experimentally and we have established that, the most optimum temperature for geological carbon sequestration is 323 K. Based on the global mean for geothermal gradient, this corresponds to approximate depth of 1600 meters.

Keywords: Aquifer; Carbonic Acid; Dissociation Constant; Fractional Flow; Geosequestration; Relative Mobility; Relative Permeability; Specific Shock; Wettability

Introduction

In line with the geological sequestration of anthropogenic carbon dioxide aimed at isolating this greenhouse gas until it becomes thermodynamically immobilized through the formation of stable carbonates [1], potential geologic repositories are depleted oil and gas reservoirs, deep un-mineable coal seams [2] salt caverns [3] fractured flood basalts and deep saline aquifers [4]. Of the potential geologic repositories, those with promising global storage potentials are deep saline aquifers [5]. In addition, geological sequestration costs are lower for deep saline aquifers [6].

While global storage potentials are of major concerns in considering potential geologic media, the two-phase flow characteristics of injected carbon dioxide and resident formation brine need to be understood. This is because, the technical optimization of sequestration projects has significant bearing on maximizing water flow velocities and minimizing injected gas flow velocities to prevent injection fluid override associated with unfavourable mobility ratio conditions [7]. Recent studies [8,9] related to wettability evolution caused by carbon dioxide interaction with rock surfaces have established that water wettability of quartz arenites (silica rich saline aquifer rocks) reduces with acidity evolution. This means that the principal cause of rock surface change from water wet to intermediate water wet is the formation of carbonic acid and its subsequent dissociation, which increases hydrogen ion activity in formation water.

Generally, trends in wettability evolution from original water wet to intermediate water wet will enhance gas injection efficiency by reducing relative permeability of injected carbon dioxide while increasing that of water. Therefore, in optimising injected gas volume in the available subsurface pore volume, seeking maximum acidity conditions will help to achieve gas injection efficiency. One way to achieve optimum acidity conditions in formation water during gas injection is to find the maximum dissociation of carbonic acid formed by hydration of injected gas under prevailing aquifer temperature and pressure conditions. In this regard, the optimum aquifer temperature for geologic storage to achieve optimum acidity conditions deserves to be investigated. The objective of this paper is to use relevant literature on the temperature dependence of carbonic acid dissociation constant for developing hypotheses on optimum storage conditions and to further find experimental proof of these hypotheses.

Literature Review

Temperature Dependence of Carbon Dioxide Activity

The activity of carbon dioxide is a function of temperature and salinity in accordance with the following equation [10]:

$$\ln\gamma_{hyd} = \left(C + FT + \frac{G}{T}\right)I - \left(E - HT\right)\left(\frac{I}{I+1}\right) \qquad (1)$$

Where

γ is the activity coefficient of the hydrated species of carbon dioxide,

T= temperature K,

I= ionic strength-mol/l,

C = -1.0312,

H = -0.001606,

F = 0.0012806,

E = 0.4445,

G = 255.9

The following figure gives the dependence of carbon dioxide activity on temperature as a function of constant salinity of aqueous solution using Equitation (1). (Figure 1) shows carbon dioxide activity decreases with increasing salinity and temperature.

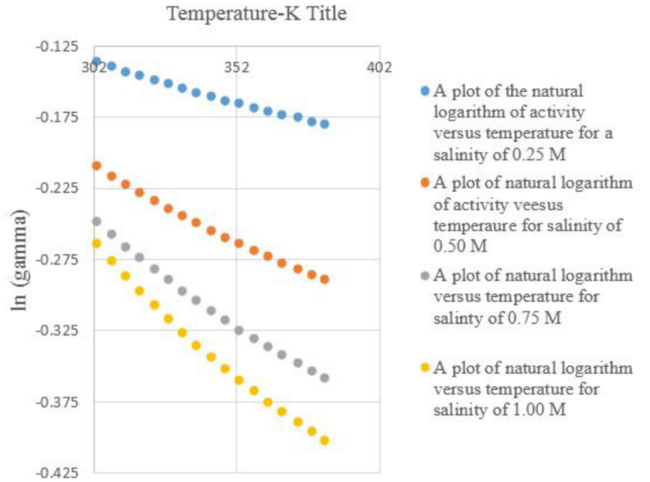

Figure 1: Dependence of carbon dioxide activity on salinity and temperature.

Acidity Evolution

The acidity evolution in formation brine during carbon dioxide injection will be due to its dissolution and dissociation. Injected carbon dioxide will hydrate in accordance with the following reaction [11,12]:

$$CO_2\text{ (gas)} + H_2O \leftrightarrows H_2CO_3 \qquad (2)$$

The hydrated product of carbon dioxide will dissociate using the apparent dissociation constant in accordance with the following reaction [11]

$$H_2CO_3 \leftrightarrows H+ + HCO_3- \qquad (3)$$

The apparent dissociation constant is given as:

$$K = \frac{\left[a_{H^+}\right]\left[a_{HCO_3^-}\right]}{\left[a_{H_2CO_3}\right]} \qquad (4)$$

K = dissociation constant of carbonic acid- mols/l

$\left[a_{H^+}\right]$= activity of hydrogen ions-mols/l

$\left[a_{H_2O_3}\right]$= activity of carbonic acid-mols/l

$\left[a_{HCO_3^-}\right]$= activity of bicarbonate ions-mol/l

In principle, the change in pH of aqueous solution is due to changes in hydrogen ion activity as indicated by Equitation (3). For there to be a significant decrease in pH of formation water during carbon dioxide injection, the dislocation products must be maximized. This can be achieved by finding an optimum temperature of the aquifer. This is because the dissolution of carbon dioxide as well as the dissociation of carbonic acid formed depends on formation water temperature and salinity. The temperature-dependent dissociation constant of carbonic acid has been shown to have a maximum value at a temperature of 323 K (50 °C) above, which decreases with increasing temperature [13]. This trend reflects a known relationship between the logarithm of the dissociation constant of carbonic acid and temperature as [14]:

$$\log K = -356.3094 - 0.060919T + \frac{21834.37}{T} + 0.8339\log\left(T_s - G_h D\right) - \frac{1684915}{T^2} \qquad (5)$$

Where

K = apparent dissociation constant of carbonic acid

T = temperature °C (Figure 2) shows a plot of dissociation constant versus temperature based on Equitation (5).

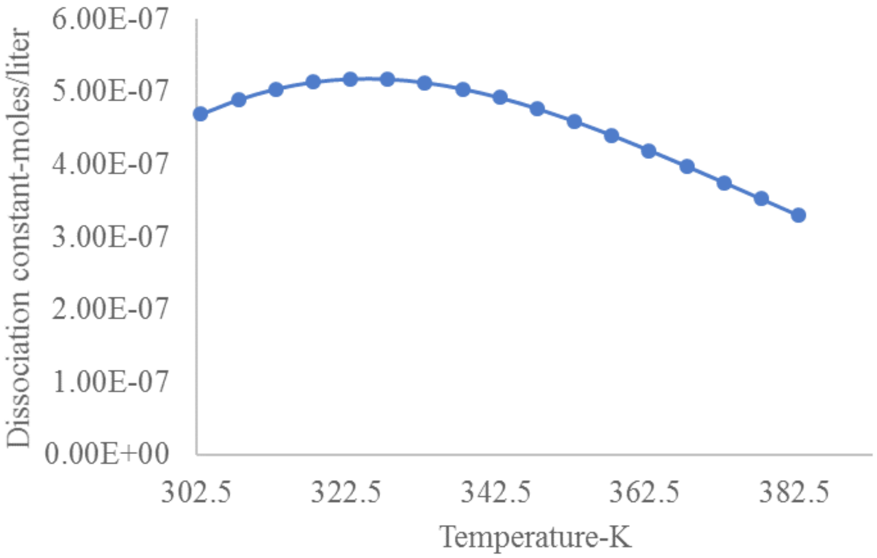

Figure 2: A plot of apparent dissociation constant of carbonic acid versus temperature (Eq. 1) showing a maximum at 323 K (50 °C).

In line with local geothermal gradient, the temperature of an aquifer increases with depth in accordance with the following equation.

$$T_D = T_s + G_h D \qquad (6)$$

Where

T_D = temperature at depth-°C

T_S = temperature at the surface-oC

G_{th} = geothermal gradient-°C/m

D = Depth-m

In principle, one way to ensure more hydrogen ion inputs from the dissociation of carbonic acid is to maximize the dissociation reaction (Equitation 3) with regard to hydrogen ion production. Since the temperature of the aquifer is depth dependent, the equation expressing the relationship between the logarithm of carbonic acid dissociation constant and temperature can be transformed into a depth dependent one. By substitution of Equitation (6) into Equitation (5), we get the following equation:

$$\log K = -356.3094 - 0.060919\left(T_s - G_h D\right) + \frac{21834.37}{\left(T_s + G_h D\right)} + 0.8339\log\left(T_s + G_h D\right) - \frac{1684915}{\left(T_s + G_h D\right)^2} \qquad (7)$$

This equation explicitly shows the dependence of carbonic acid dissociation constant on aquifer depth.

Optimum Depth of Geological Sequestration

From (Figure 2), the maximum dissociation constant of carbonic acid occurs at 323 K (50 °C). This permits calculation of the optimum depth as:

$$D = \left(\frac{T_D - T_s}{G_h} \right) \quad (8)$$

Assuming a mean geothermal gradient value of 25 °C km^{-1}, this can be written as:

$$D = \left(\frac{T_D - T_s}{25} \right) \quad (9)$$

Using a mean surface temperature of 283 K (10 °C), this gives:

$$D = \left(\frac{50 - 10}{25} \right) = 1.6 \quad (10)$$

Mechanism of Carbon Dioxide Induced Dewetting of Aquifer Rocks

For multiphase flow in porous media, the wettability of a solid surface with regard to a particular phase fluid is the preference of this phase for the solid surface [15]. This wetting preference is measured by the wettability index [16]. Analogous to Amos Wettability Index for wettability quantification is the cosine of the contact angle which measures wettability in terms of interfacial free energies or interfacial tensions. This equation is given as:

$$\cos\theta = \frac{\sigma_{sv} - \sigma_{sl}}{\sigma_{lv}} \quad (11)$$

Where

θ = contact angle-degrees

σ_{sv} = solid-vapor interfacial tension-N/m

σ_{lv} = liquid-vapor interfacial tension-N/m

σ_{sl} = solid-liquid interfacial tension-N/m

Equation 11 shows that contact angle for carbon dioxide-rock-brine systems will change with changes in interfacial intension. In the carbon dioxide-brine-rocks system, the principal cause of wettability variation is the change in solid-liquid interfacial tension. This change in interfacial tension can be brought about physically due to roughening of solid surface [18] and chemically due to surface reactions involving surface charged sites [19]. Considering the surface of saline aquifer rocks as containing surface hydroxyl functional groups such as silanol [20], the following reaction can be written to represent the surface conditions of saline aquifer rocks, particularly sandstones, prior to gas injection [21]:

$$\equiv SOH \rightarrow \equiv SO^- + H^+ \quad (12)$$

Where:

$\equiv SOH$ = surface neutral species

$\equiv SO^-$ = surface deprotonated species

H^+ = hydrogen ion

This reaction describes a deprotonation reaction where a surface hydroxyl functional group desorbs proton leading to a negative surface site represented by . $\equiv SO^-$

Intermolecular Forces Effect On Interfacial Tension

The interfacial tension between two phases results from intermolecular interactions [22]. These forces are van Der Waals forces and forces of electrostatic origin. The electrostatic contributions also called electron donor and electron acceptor components of interfacial tension result from surface charge sites. These surface charge sites develop depending on the pH of aqueous solution in contact with a solid surface and the point of zero charge pH of the solid surface; such phenomena being associated with amphoteric surface behaviour [23]. In this regard, Equitation (12) is the representative geochemical reaction of aquifer rock surface in contact with an aqueous solution of a given pH above the point of zero charge pH of rock mineral surface. Under such conditions, the solid-liquid interfacial tension in Equitation (11) can be written as [24]:

$$\sigma_{sl} = \left(\left(\sigma_s^{LW}\right)^{1/2} - \left(\sigma_l^{LW}\right)^{1/2} \right)^2 + 2\left(\left(\gamma_s^+ \gamma_s^-\right)^{1/2} + \left(\gamma_l^+ \gamma_l^-\right)^{1/2} - \left(\gamma_s^+ \gamma_l^-\right)^{1/2} - \left(\gamma_s^- \gamma_l^+\right)^{1/2} \right) \quad (13)$$

Where:

σ_{sl} = interfacial tension between rock surface (s) and brine (l)-N/m

σ_s^{LW} = a polar component of solid-liquid interfacial tension coming from rock Surface-N/m

σ_l^{LW} = a polar component of solid-liquid interfacial tension coming Brine-N/m

σ_s = surface tension of rock Surface-N/m

σ_l = surface tension of Brine-N/m

γ_s^+ = electron acceptor component of solid-liquid interfacial tension coming from solid surface –N/m

γ_s^- = electron donor component of solid-liquid interfacial tension coming from solid Surface-N/m

γ_l^+ = electron acceptor component of solid-liquid interfacial tension coming from Brine-N/m

γ_l^- = electron donor component of solid-liquid interfacial tension coming from Brine-N/m

In line with Equitation (13), the electron donor component coming from the solid surface represents the negatively charged surface site while the electron acceptor component comes from the positively charged sites. Consequently, the effect of acidity evolution in saline aquifers can be realized from inspection of Equitation (13). This means, as injected carbon dioxide dissolves leading to increased hydrogen ion concentration in brine, the reaction described by Equitation (12) will move to the right in accordance with Lech atelier's principle [25,26] resulting in protonation of surface sites. This corresponds to decrease in electron donor contribution to solid-liquid interfacial tension described by Equitation (13). For zero negatively charged sites on rock surface, Eq. (13)

$$\sigma_{sl} = \left(\left(\sigma_s^{LW}\right)^{1/2} - \left(\sigma_l^{LW}\right)^{1/2}\right)^2 + 2\left(\left(\gamma_l^+ \gamma_l^-\right)^{1/2} - \left(\gamma_s^+ \gamma_l^-\right)^{1/2}\right) \tag{14}$$

By inspection of Equations (13) and (14) it is clear that the effect of increasing pH is to increase solid-liquid interfacial tension since all terms containing electron donor contribution of rock mineral surface contain negative signs. At the point of zero charge pH of aqueous solution, which is the pH at which the net surface charge is zero [27], Equitation (14) becomes:

$$\sigma_{sl} = \left(\left(\sigma_s^{LW}\right)^{1/2} - \left(\sigma_l^{LW}\right)^{1/2}\right)^2 + 2\left(\left(\gamma_l^+ \gamma_l^-\right)^{1/2}\right) \tag{15}$$

Equation (15) indicates that at the point of zero charge pH of rock surface, the interfacial tension between solid and liquid depends only on the polar contribution from liquid.

For an ionisable rock surface, the solid-liquid interfacial tension can further be decomposed into two main parts as follows [28]:

$$\sigma_{sl} = \sigma^o + \sigma^{ion}\left(pH\right) \tag{16}$$

Where:

σ_{sl} = solid-liquid interfacial tension

σ^o = contribution to solid liquid interfacial tension at the point of zero charge pH-N/m

σ^{ion} = contribution to solid-liquid interfacial tension from ionized site at a given pH of aqueous solution relative to the pH of point of zero Charge-N/m. This corresponds to the free energy of formation of ionizeable surface relative to the point of zero charge pH.

Effect of pH on Contact Angle

From Equitation (11) and the pH dependence of solid-liquid interfacial tension given by Equitation (16), contact angle dependence on pH can be given as:

$$\cos\theta = \frac{\sigma_{sv} - \sigma_{sl}\left(pH\right)}{\sigma_{lv}} \tag{17}$$

Since the effect of decreased pH is to increase solid-liquid interfacial tension as explained in the previous section, decreasing pH corresponds to decreasing the cosine of the contact angle, which correlates with the system's wettability. This trend has been reported in recent research findings [9,29,30]. These findings reflect the explanations given in the previous section in connection with solid-liquid interfacial tension dependence on pH.

Fractional Flow Theory

When two or more immiscible phases flow in a porous medium, the fractional flow of a phase is defined as the fraction of the total flux that is assigned to that phase. For multi-phase flow in porous media, the fraction of a phase in the porous medium in the absence of capillary effects is given as [31]:

$$f_1 = \frac{1}{1 + \frac{k_{r2}}{\mu_2} * \frac{\mu_1}{k_{r1}}} \tag{18}$$

In this equation, *f1, kr1, kr2, μ1 and μ2* are fractional flow of phase 1, relative permeability of phase 1, relative permeability of phase 2, dynamic viscosity of phase 1 and dynamic viscosity of phase 2 respectively.

The fractional flow of phase 2 is given as Equitation (19).

$$f2 = 1 - f1 \tag{19}$$

f2=fractional flow of phase 2.

For drainage flow characteristic of carbon dioxide injection, the fractional flow of gas is given as:

$$f_{CO_2} = \frac{1}{1 + \frac{k_w}{\mu_w} * \frac{\mu_{CO_2}}{\mu_{w_2}}} \tag{20}$$

In this equation, f_{co2}, k_{rCO2}, k_{rw}, μ_{CO2} and μ_w represent fractional flow of carbon dioxide, relative permeability of carbon dioxide (fraction), relative permeability of water (fraction), dynamic viscosity of carbon dioxide and dynamic viscosity of water respectively.

Effect of Fractional Flow On Phase Relative Mobility

The relative permeability of a phase in the porous medium reflects the wettability of the system, which further determines the flow and distribution of that phase [32]. Generally, the higher the fractional flow of a phase, the less wetting is that phase to the solid surface and the greater its mobility. Considering of carbon dioxide injection into saline aquifers, the fractional flow of resident water is the fraction of the total flow at a given point in the aquifer that is due to water flow. As the wettability of the system decreases due to pH effect, the fractional flow of water will tend to increase, and this means an increase in water relative mobility, resulting in more efficient displacement of water. This is because the relative mobility of a fluid phase depends on whether it wets the solid (low relative mobility) or whether it is non-wetting with regard to the solid (high relative mobility) [33].

Generally, decreasing water relative mobility also means less carbon dioxide relative mobility which tends to move directly behind the displacing water. In the petroleum industry, alteration of wettability in zones around gas condensate well bores to intermediate gas wetting has been used to improve gas deliverability by inducing higher condensate mobility in these zones [34]. In this regard, the effect of wettability alteration is to increase water relative mobility and fractional flow in zones around well bores. Consequently, the effect of wettability on the specific shock velocity of injected carbon dioxide is central to the displacement and we will endeavour to explain this in the following section.

Effect of Wettability On Specific Shock Velocity

The frontal advance theory of Buckley and Leveret is well known in the petroleum industry improved oil recovery schemes involving water flooding of petroleum reservoirs [35]. As carbon dioxide is injected into a saline aquifer, a shock develops due to the sudden increase of the initial injected gas saturation in the porous medium to a frontal saturation similar to that encountered in water flooding of petroleum reservoirs where initial saturation jumps from irreducible water saturation to a frontal water saturation. This jump, which is characterized by an initial injected fluid saturation in the porous medium (S_{w1}) to a frontal saturation (S_{w2}) is influenced partly by the wettability of the system (See Figure 3) and partly by the injection fluid flux. The jump is further characterized by a specific shock velocity calculated as [36]:

$$v_{\Delta S_w} = \frac{q}{A\phi} * \frac{f_{w2} - f_{w1}}{S_{w2} - S_{w1}} \tag{21}$$

$v_{\Delta S_w}$ = specific shock velocity-ms^{-1}

q = total injection rate-m^{3}s^{-1}

A = cross sectional area of injection-m^2

ϕ = sediment porosity-fraction

f_{wi} = fractional flow of injected fluid at initial saturation (S_{wi}) in the porous medium

f_{w2} = fractional flow of injected fluid at initial saturation (S_{wi}) in the porous medium

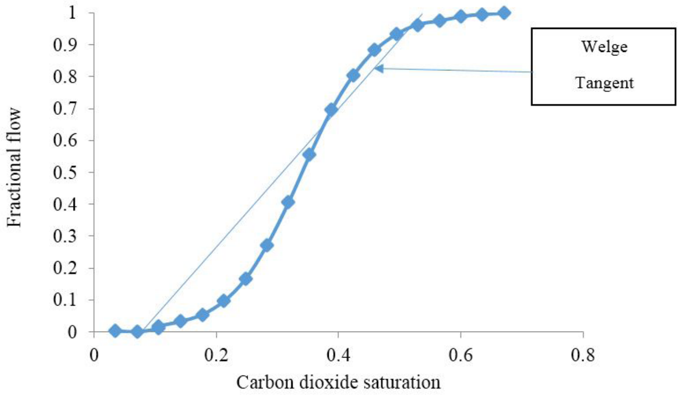

Figure 3: A typical plot of water fractional flow versus water saturation with Welge tangent.

From (Figure 3), the gradient of the tangent, which starts from the point (S_{wi}, fw_1), and touches the fractional flow curve at the point (S_{w2}, f_{w2}), is calculated using the tangent. This is Welge's tangent [37]. Generally, the less wetting the resident fluid is to the porous medium, the lower the gradient of the tangent and the lower is the specific shock velocity and the higher the injected phase saturation at breakthrough. Therefore, in the carbon dioxide-brine system, pH decrease caused by carbon dioxide dissolution and the increase in solid-liquid interfacial tension as explained in Section 2.4.1, will cause dewetting of solid surface with regard to rock mineral surface as observed experimentally by [9,29]; this will cause water to have increased relative mobility. Consequently, the higher the hydrogen ion concentration the higher will water relative permeability be and the better the injection sweep efficiency.

Hypotheses

Putting together acidity generation in saline aquifers due to carbon dioxide dissolution in formation brine, the dependence of the dissociation constant of carbon dioxide on temperature as well as the dependence of solid-liquid interfacial tension on pH, the following hypotheses are proposed and tested experimentally using relevant experimental data:

- At a temperature of 323 K from Figure 2, the dissociation of carbon dioxide in brine and the activity of hydrogen ion in brine will be at a maximum. This means that the interfacial tension between rock and brine and the contact angle will be at a maximum leading to a condition of lowest system wettability.
- At a temperature below 323 K, the activity of hydrogen ion in solution is lower than that at 323 K, meaning lower solid-liquid interfacial tension resulting in lower contact angle and higher wettability.
- As temperature increases towards 323 K, increase hydrogen ion concentration in brine means decreasing pH and increasing solid-liquid interfacial tension. This means increasing water fractional flow at the expense of fractional carbon dioxide, which translates to decrease relative mobility of carbon dioxide.
- Decreasing relative mobility of injected carbon dioxide means decreasing specific shock velocity of injected carbon dioxide.
- Decreasing specific shock velocity of injected carbon dioxide coupled with decreasing water wetness means increasing displacement efficiency and decreasing residual water saturation as temperature increases towards 323 K.

The implication of the above hypotheses is that for quartz arenites (quartz rich sedimentary rocks) [38] where wettability evolution is eminent [29]; and where decrease in water wettability of the aquifer rocks can occur to enhance better sweep efficiency, the ideal temperature where maximum dissociation of carbonic acid will occur to cause maximum wettability decrease is 323 K and this corresponds to a depth of 1600 meters based on a mean global geothermal gradient of 25 degrees per kilometre of depth [39]. These hypotheses will be tested using experimental data.

Testing of Hypotheses Using Experimental Data

Characterization of Core Samples: Four core samples were drilled from a chunk of Wallace Sandstone procured from the quarry. The drilling was done using water as a lubricating fluid. The long drilled core was then cut into four core samples with length 78 mm and diameter 39 mm, using oil as the lubricating fluid. The cores were then cleaned by flushing with a mixture of methanol and toluene using the Bench Top relative permeameter manufactured by Vinci Technology of France (See Figure 4). Specifically, every core was subjected to one litre of injection followed by one litre of distilled water injection to rinse it. Following the cleaning, the cores were dried in an oven overnight for one night at a temperature of 353 K to avoid any thermal decomposition of core components. They were then removed and left to cool to ambient temperature.

Figure 4: Setup of Bench top relative permeameter.

Porosity Determination: Porosities were determined using the imbibition saturation method [40]. The cores were first weighed, then put in beakers of brine and left in a vacuum for 24 hours to achieve full saturation. The fully saturated cores were then weighed. The density of brine at room temperature was measured. To calculate porosity, the following equation was used:

$$V_p = \frac{W_{ww} - W_{dw}}{\rho_b}$$

$$\phi = \frac{V_p}{V_b} * 100$$

Where:

V_p = pore volume

V_b = bulk volume

W_{wt} = wet weight

W_{dw} = dry weight

ϕ = porosity

Brine Preparation: Experimental brine was prepared based on a salinity of 48,000 ppm similar to that of the Basal Cambrian Sandstone [41-43]. Sodium chloride with laboratory grade (99.9) was purchased from Sigma Aldrich and used without further purification. The sodium chloride was weighed using Ohaus Adventurer Balance Scale manufacture by ULINE, that measures weight up to 820 grams with a precision of 0.01 gram.

Permeability Determination: Absolute permeabilities were determined using the universal Core Flooding System (CFS) (Figure 5-7) manufactured by Vinci Technologies (Appendix 1) for experimental capabilities). After the core was loaded into the Hassler core barrel, radial stress corresponding to overburden stress was put on. The brine accumulator was filled with the experimental brine. Experimental conditions of temperature were then imposed using the oven facility and permeability tests were carried out. The basis for monophasic permeability determination is Darcy law. Therefore, a software records pressure drop versus flow rate. At the end of each test, a graph of pressure drop versus flow rate was automatically plotted together with a display of computed permeability using the gradient of the plot (Appendix 2). (Table 1) shows the detailed characterization results.

Core diameter	1.5"
Core length	2"-12"
Wetted material	C-276 Hastelloy and Titanium TA6V
Maximum pore pressure	10,000 psi
Maximum confining pressure	10,000 psi
Temperature range	Up 150 degrees Celsius
Maximum number of test fluids	Up to three fluid (gas, brine and oil)
Electrical voltage	230 VAC, 50/60 Hz. One phase

Appendix 1: System Capability.

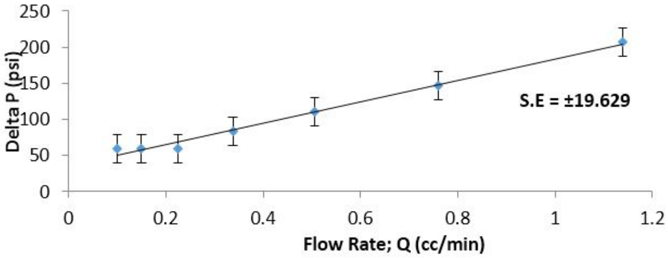

Plot for experiment at 323 K (50 ^{0}C).

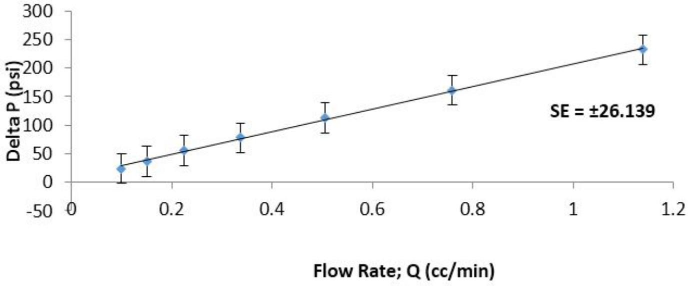

Plot for experiment at 333 K (60 0C).

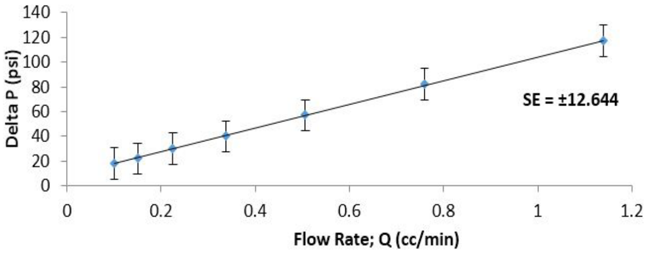

Plot for experiment at 343 K (70 0C).

Appendix 2: Monophasic permeability experimental data plots at.

Experimental Condition Temp. K	Length cm	Diameter cm	Porosity-fraction	Permeability -mD	Permeability - *$10^{-9\ m2}$
323	78	39	12.25	1.87	1.85
333	78	39	13.55	1.75	1.73
343	78	39	12.55	1.85	1.83

Table 1: Measured petrophsyical data on Wallace Sandstone core samples.

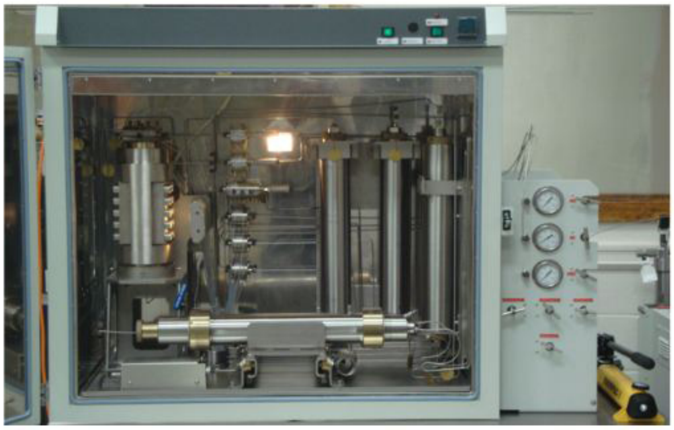

Figure 5: Inner view of the Universal Core Flooding System with accumulators, core holder and separator.

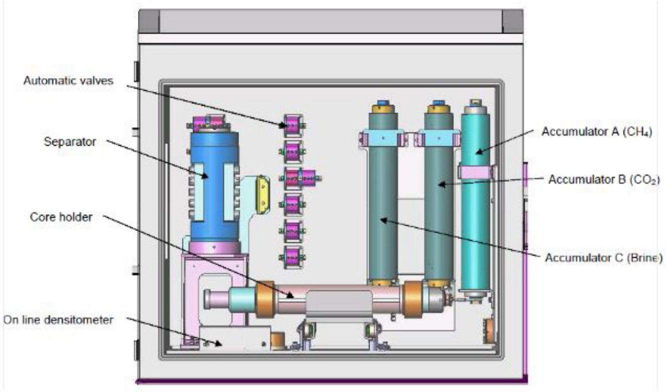

Figure 6: Test Chamber of CFS with accumulators, separators and Hassler core holder.

Figure 7: Universal Core Flooding System with pumps and computer monitoring system.

Relative Permeability Measurement

Test Conditions

We assumed a sequestration depth with salinity similar to that used by [41,42]. Accordingly, the depth of aquifer was taken as 2734 meters. We assumed a normal pore pressure at this depth, based on a normal pore pressure gradient of 0.465 psi per foot [44]. Calculation of aquifer pressure at the chosen depth gives a pore pressure of 26 MPa (3814 psi). Using an overburden gradient of 1 psi per foot [45] we calculated the overburden pressure as 57 MPa (8202 psi). Three test temperatures were selected to be 323 K, 333 K and 343 K. (Table 2) shows the dynamic viscosities measure under different temperature conditions using the viscometer of the universal core flooding system [46].

Temperature (K)	Pore pressure-(MPa)	Overburden pressure-(MPa)	Salinity	Brine viscosity (cp)	Gas viscosity (cp)
323	26	57	248	0.840	0.076
333	26	57	248	0.754	0.068
343	26	57	248	0.708	0.062

Table 2: Test Conditions.

Saturating A Phases with an Immiscible Component

In measuring relative permeability, we adopted the procedure of the Global Carbon Capture and Storage Institute [47]. Before the start of the core-flooding test, the brine and CO_2 had to be mutually saturated with each other under in-situ reservoir conditions. Below are the steps which outline the procedure followed to make sure that brine and CO_2 became fully saturated with each other before the drainage test: The brine accumulator and CO_2 accumulator were cleaned, vacuumed and filed with their respective fluids.

The experimental brine was deaerated. All of them were brought to reservoir conditions of temperature and pressure. Next, the accumulators were isolated and CO_2 was brought into contact with brine by opening the relevant valves while using the lines connecting the two accumulators (Figure 8). While connecting the bottles, one of the injection pumps was used to inject about 200 cc of brine into the CO_2 accumulator following which 10 to 15 minutes were allowed for brine to settle in the carbon dioxide accumulator. The same amount of carbon dioxide was injected into the brine accumulator to form a gas cushion above the injected brine in the accumulator. The system was then left for five days for carbon dioxide to diffuse into the brine and for brine at the bottom of the CO_2 to evaporate into the CO_2. In this regard, convective mixing enhanced the diffusion of CO_2 into the brine, thereby creating a homogeneous mixture [48,49].

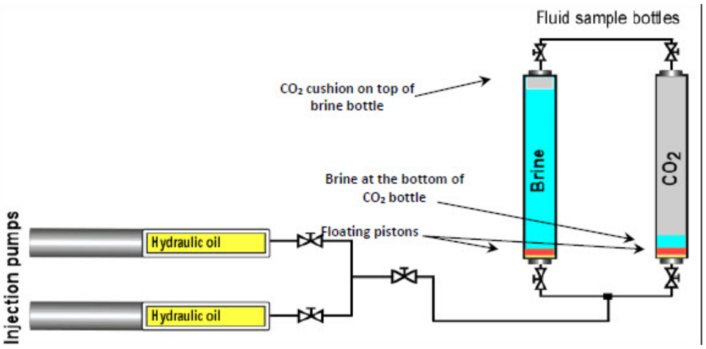

Figure 8: Schematic of fluid phase in contact with each other.

During all the above procedures, one of the injection pumps was left connected to the CO_2 while operating under constant reservoir pressure. The two accumulators were also maintained at reservoir temperature, which was set by regulating oven temperature. The CO_2 accumulator was finally isolated by closing the valve connected to the top. All the lines including the one in the stainless steel cylindrical sample were vacuumed and filled with dead formation brine and then pressurized to reservoir pressure (pore pressure). The fluid inside the brine accumulator was injected to displace the dead brine into the separator, which was at the same reservoir conditions of temperature and pressure. As soon as brine production was detected, the CO_2 collection pump was set to operate at constant reservoir pressure. Any time there was a decrease in the volume of CO_2 in the CO_2 collection pump, it was a direct indicator that more CO_2 was being dissolved in the produced brine in the separator and this warranted leaving CO_2 and brine in contact for some more days to achieve saturation. However, if the volume of CO_2 in the CO_2 collection pump did not change, it was an indicator that brine was fully CO_2 saturated. The procedures involved in saturating brine with CO_2 were repeated until full saturation was achieved. The CO_2 phase became saturated with brine vapor soon after brine was injected into the bottom of the CO_2 accumulator.

Carrying Out Absolute and Relative Permeability Tests

The core sample to be rested was carefully wrapped in a sleeve before loading it into the core holder. A hand pump (Figure 9) was used to provide the overburden pressure between the outer diameter of the sleeve and the inner surface of the core holder shell. The overburden pressure was gradually increased to the full reservoir effective pressure and all the outlet and inlet ports of the core holder were connected to the appropriate flow lines and pressure measuring devices. The core samples were injected using a low pressure 300 psi-(2.07 MPa). This enables the high diffusivity of carbon dioxide to be exploited for replacing any trapped air in the sample. The advantage of this experimental procedure is that carbon dioxide, which replaces air in the core, is easily removed from the core when required.

The remaining carbon dioxide can also dissolve in the saturated dead brine. Following the initial flushing of the samples by carbon dioxide, all the flow-lines and the core samples were flushed overnight using a vacuum pump. The backpressure was then brought to full reservoir pressure while maintaining oven temperature at reservoir conditions. The core samples were then displaced saturated with dead experimental brine while maintaining confining pressure equal to reservoir pressure. To become completely saturated with dead brine the sample was left under this condition for 48 hours. Apart from being completely saturated with dead brine this procedure enabled adsorption equilibrium.

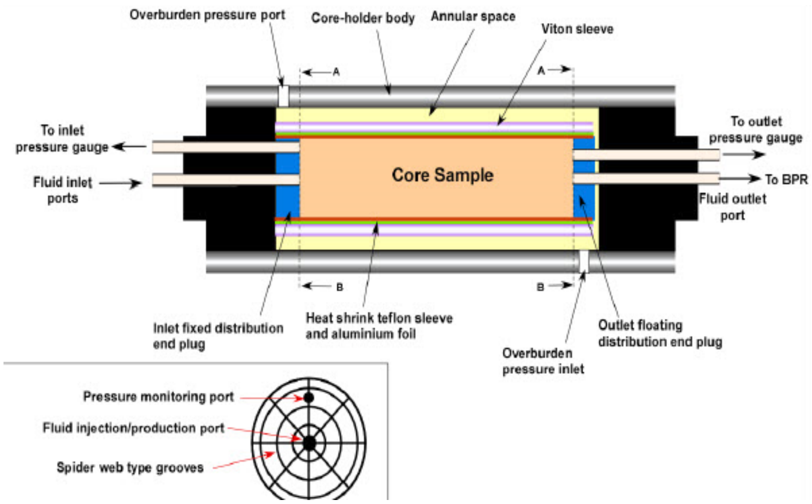

Figure 9: Schematics of Hassler core holder with core and vital components including sleeve.

Next, the carbon dioxide saturated brine was injected into the core sample using a constant flow rate to displace the dead formation brine. Injection was continued until a steady state was achieved, where the differential pressure was constant and fluid production rate was equal to fluid injection rate. Before steady state was achieved, a plot of pressure drop versus flow rate was automatically recorded by the software, Cyder, which controls the injection process. A plot of pressure drop versus flow rate using Darcy's law enables Cyder to use the gradient of the plot to automatically calculate and display permeability.

To carry out relative permeability tests, the vapor saturated carbon dioxide was injected at a pressure and displacement continued until irreducible water saturation was achieved, where constant differential pressure was achieved. During the test, Cider recorded differential pressure and fluid production with time and automatically plotted graphs of these at the end of the test (Appendix's 3,4). During drainage experiments, the injection rate of carbon dioxide took place at pore pressure. Injection was carried out until flood out when irreducible water saturation was attained. While injection continued, a video camera enabled tracking of the interface between produced brine and gas. At flood out, there was no more interface movement no matter the length of time involved in injection. Using this approach flooding experiments were conducted for temperatures 323 K, 333 K and 343 K

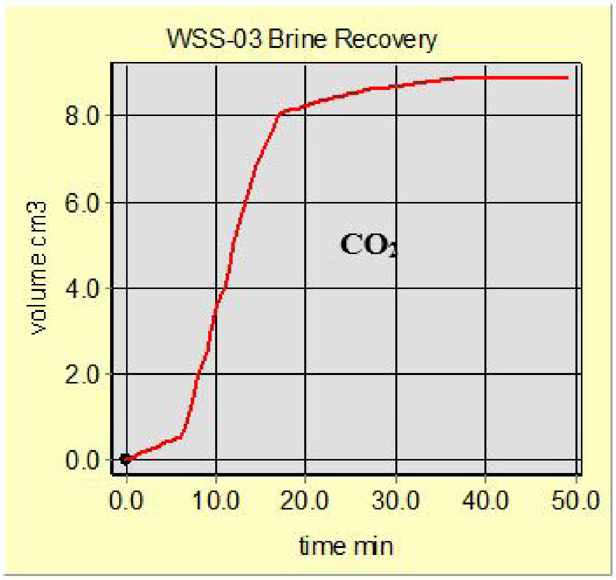

Recovery plot at 323 K (50 ^{0}C)

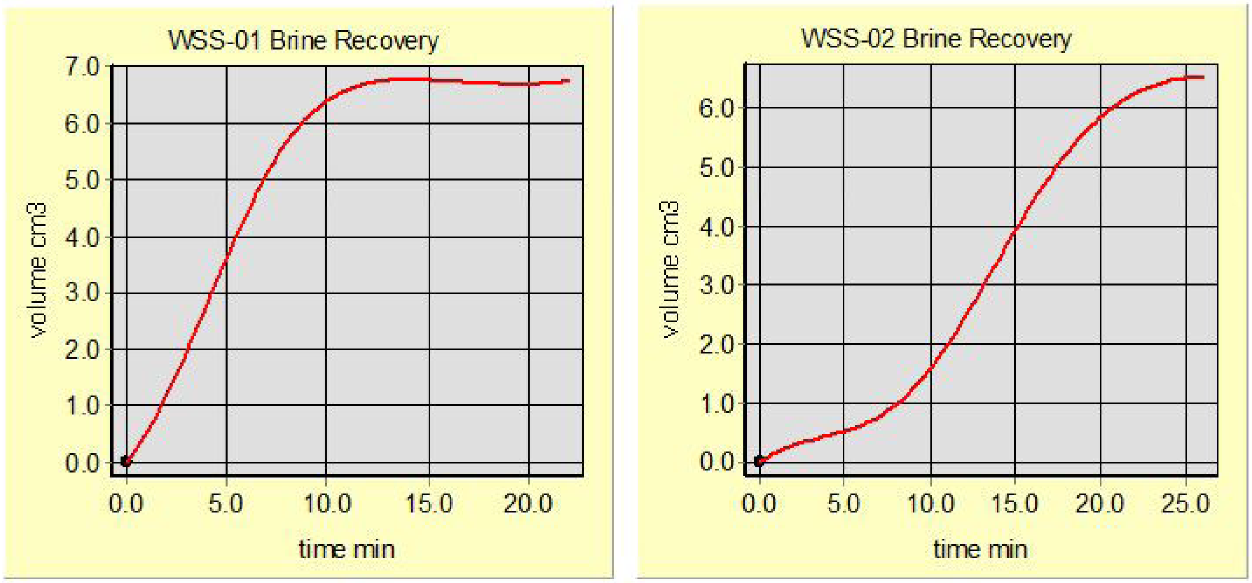

Recovery plots at 333 K (60 ^{0}C)

Recovery plot at 343 K (70 ^{0}C)

Appendix 3: Experimental data plots for brine recover.

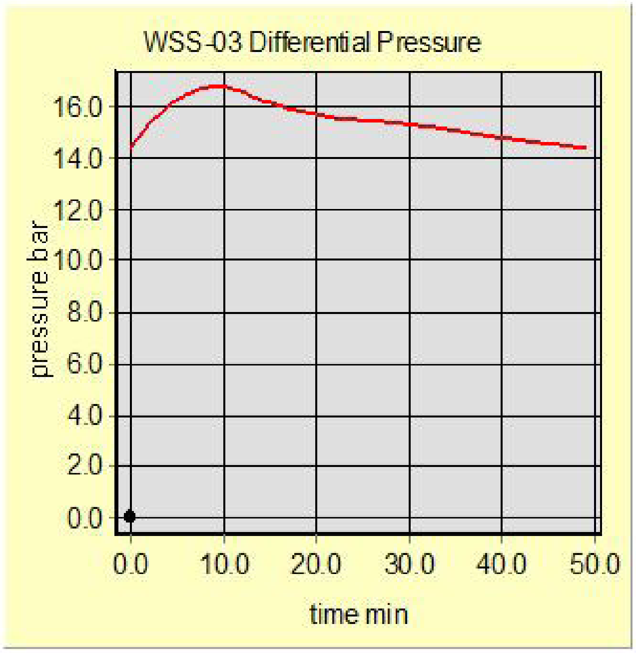

Differential pressure plolt for exp. @323 K

Differential pressure plot for exp. @ 333 Kx

Differential pressure plot for expt.@ 343 K

Appendix 4: Differential pressure plots for different experiments.

Relative Permeability Computation Using Test Data

Relative permeability computation using Cyder requires information on core length, porosity, diameter time of injection fluid breakthrough obtained from pressure drop versus time plot (Appendix 4) and fluid produced at injection breakthrough obtained from fluid production versus time plot (Appendix 3). The time to breakthrough was obtained from the point of the graph of Appendix 4 where there was a sharp drop in differential pressure. This was used to obtain the volume of brine recovered from (Appendix 3). By putting all required information, the software carries out relative permeability calculation using a numerical approach based on the JBN theory [50]**.** Appendices 6 Show the results of relative permeability tests.

Results and Discussion

(Table 3) shows cumulative volumes of brine obtained at different experimental temperatures. The table shows that maximum brine (8.811 cm^3) was recovered at 323 K. This was followed by experiment at 333 K with a recovery of 6.728 cm^3. The least recovery was that associated with experiment at 343 K. According to Anderson [33], the phase that is less wetting with regard to the solid surface will have the highest relative mobility and in case this is the resident fluid, then it will be easily displaced by the invading fluid. From our theory of acid induced solid-liquid interfacial tension change, the solid-liquid interfacial tension at 323 K will be a maximum because the maximum dissociation of carbonic acid will provide more hydrogen ions to drive the surface protonation reaction (13). In accordance with Young's equation relating contact angle to interfacial tensions the increased solid-liquid interfacial tension means decrease cosine of the contact angle. This corresponds to decreased water wettability of solid or mineral surface. The relative mobility of brine was, therefore, highest at 323 K. This explains the efficient brine displacement at 323 K, which reflects the result in (Table 3).

Temperature (K)	Cumulative Brine Production (cm^3)	Recovery Time (min)	Breakthrough Time (min)
323	8.811	37	9
333	6.728	22	7
343	6.595	26	12

Table 3: Summary of Brine Recovery and Differential Pressure Plots from Drainage Experiments.

One of the important factors is the solubility of carbon dioxide which depends on pressure, temperature and salinity [51]. Generally, it deceases with temperature and salinity and increases with pressure at a given temperature and salinity. In our experiments, we maintained the same injection pressure and salinity. Therefore, the only parameter that influenced solubility was temperature. Consequently, there was more dissolved carbon dioxide at 323 K to produce increased acidity compared to experiments at 333 K and 343 K. On the basis of the explanations given regarding temperature, one would expect experiment at 333 K to be next with regard to brine recovery and this proves to be the case in (Table 3).

Also, the other factors to consider are the absolute permeabilities of the cores. In this regard, Table 1 shows that the permeabilities of the cores are quite close and, assuming negligible grain expansion at all temperatures, the influence of permeability on brine was negligible. The dynamic viscosities of the brine as shown in (Table 4) are 0.840, 0.754 and 0.708 for experiments at 323 K, 333 K and 343 K respectively. Differences in dynamic viscosities were quite minimal. Therefore, the results of brine displacement prove our hypotheses that at 323 K maximum dissociation of carbonic acid will induce higher solid-liquid interfacial tension change to cause lower water wettability and higher brine relative mobility leading to higher displacement efficiency. Results at higher temperatures also support our hypotheses.

(Table 4) also shows that irreducible water saturation at 323 K was the lowest followed by the value at 333 K with that at 343 K being the highest. Accordingly, the relative permeability of carbon dioxide at irreducible water saturation called end point relative permeability was quite higher at 323 K, meaning the relative mobility of carbon dioxide was lowest at this temperature and this enhanced the displacement efficiency as carbon dioxide moved directly behind brine with less chances of injection override. Experiment at 333 K had the next higher value and that at 343 K has the least value. All these trends reflect decreasing displacement efficiency as seen in (Table 3).

Temperature (K)	Relative permeability of CO_2 at irreducible brine saturation	Irreducible brine saturation-fraction	Dynamic viscosity of brine-*10^{-5} (Pa·s)	Dynamic viscosity of CO_2-*10^{-5} (Pa·s)	Viscosity ratio-CO_2/Brine
323	0.534	0.402	840	1.61	1.9
333	0.254	0.712	75.4	1.63	21.7
343	0.388	0.737	70.8	1.66	24.3

Table 4: Summary of Relative Permeability and Saturation Data from Drainage Experiments.

(Figure 10) shows a graph of relative permeability of phases obtained from relative permeability measurements (Appendix 5-7). The relative permeability of a phase is its ability to move relative to the other phase or phases present in the porous medium. The figure shows that the relative permeability of brine was highest at 323 K. Experiment at 333 K produced a graph with the next highest. Relative permeabilities were lowest for experiment at 343 K. All these observations support our hypotheses. Results for carbon dioxide reflect these same trends and, accordingly, support our hypothesis that the relative mobility of carbon dioxide will increase with temperature increase. Accordingly, the relative mobility of carbon dioxide was generally lower at 323 K (50 ^{0}C) and generally higher at 343 K (70 ^{0}C).

Sw	krw	krCO$_2$	Fractional flow of water	Fractional flow of carbon dioxide
0.988	0.96	0.001	0.946417	1.41E-05
0.903	0.703	0.025	0.471819	0.008221
0.855	0.574	0.046	0.272791	0.024139
0.801	0.444	0.076	0.132205	0.05337
0.752	0.343	0.108	0.064252	0.087769
0.704	0.255	0.146	0.028688	0.129575
0.656	0.18	0.19	0.01158	0.177776
0.553	0.064	0.305	0.00096	0.300425
0.451	0.007	0.452	7.86E-06	0.451493
0.42	0.001	0.503	1.44E-07	0.502927

Appendix 5: Relative permeability and fractional flow data for experiment at 323 K.

Sw	krw	krCO$_2$	Fractional flow of water	Fractional flow of carbon dioxide
0.997	0.98	0.002	0.953197	5.47E-05
0.991	0.94	0.007	0.852528	0.000651
0.953	0.703	0.04	0.394066	0.017578
0.907	0.458	0.079	0.13564	0.055604
0.854	0.245	0.124	0.030727	0.108448
0.837	0.189	0.139	0.016976	0.126515
0.802	0.098	0.168	0.003981	0.161176
0.773	0.045	0.193	0.000749	0.189788
0.752	0.02	0.21	0.000137	0.208558
0.723	0.002	0.235	1.23E-06	0.234855
0.72	0.001	0.238	3.05E-07	0.237927

Appendix 6: Relative permeability and fractional flow data for experiment at 333 K.

Sw	krw	krCO$_2$	Fractional flow of water	Fractional flow of carbon dioxide
0.992	0.94	0	0.94	-----------
0.947	0.637	0.016	0.473227	0.004114
0.899	0.38	0.057	0.123911	0.038413
0.865	0.235	0.103	0.033386	0.088367
0.801	0.059	0.222	0.001117	0.217799
0.791	0.041	0.247	0.000488	0.24406
0.759	0.007	0.327	1.09E-05	0.326493
0.753	0.004	0.342	3.39E-06	0.34171
0.751	0.003	0.349	1.87E-06	0.348782
0.748	0.002	0.357	8.13E-07	0.356855
0.745	0.001	0.364	1.99E-07	0.363927

Appendix 7: Relative permeability and fractional flow data for experiment at 343 K.

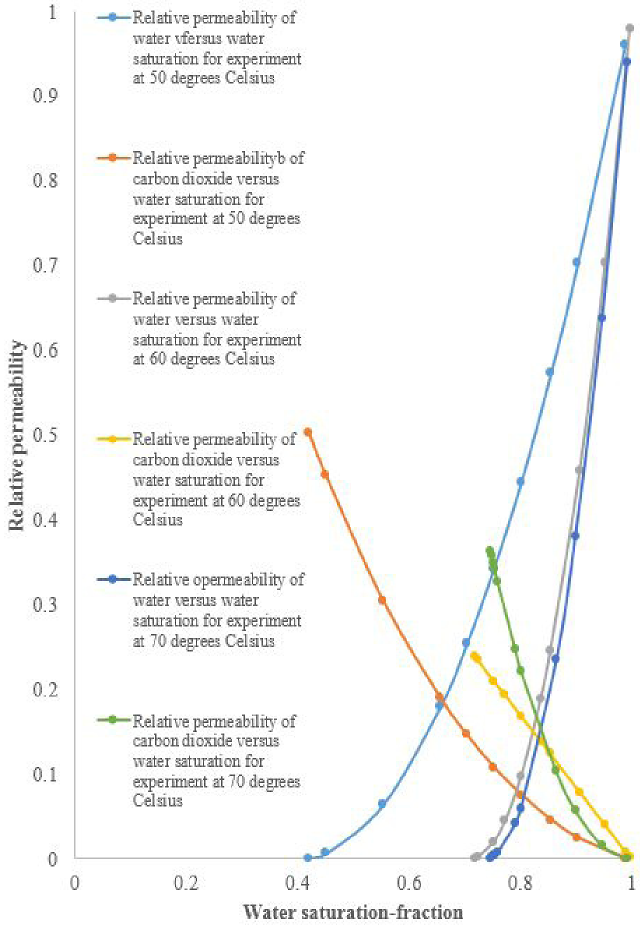

Figure 10: Relative permeability of water and carbon dioxide at experiments at different temperatures.

Regarding fractional flow, values for the injected fluid is the most relevant to explain displacement efficiencies. (Figure 11) shows at plot of fractional flow of injected carbon dioxide versus carbon dioxide saturation. Data for the plots were obtained using relative permeability and dynamic viscosity data reported in Appendix 6 and Table 4 respectively. Equation (18) and Equation (19) were used for fractional flow calculation. Generally, for a two-phase flow, a phase with lower fractional flow experience lower relative mobility or relative permeability. On the basis of our hypotheses, carbon dioxide must have a lower fractional flow at a lower temperature 323 K (50 oC) and this is evident in the fractional flow curve at 323 K. Consequently, the curve for 343 K (70 oC) shows higher fractional flow with the exception of a portion of it. All these trends support our hypotheses.

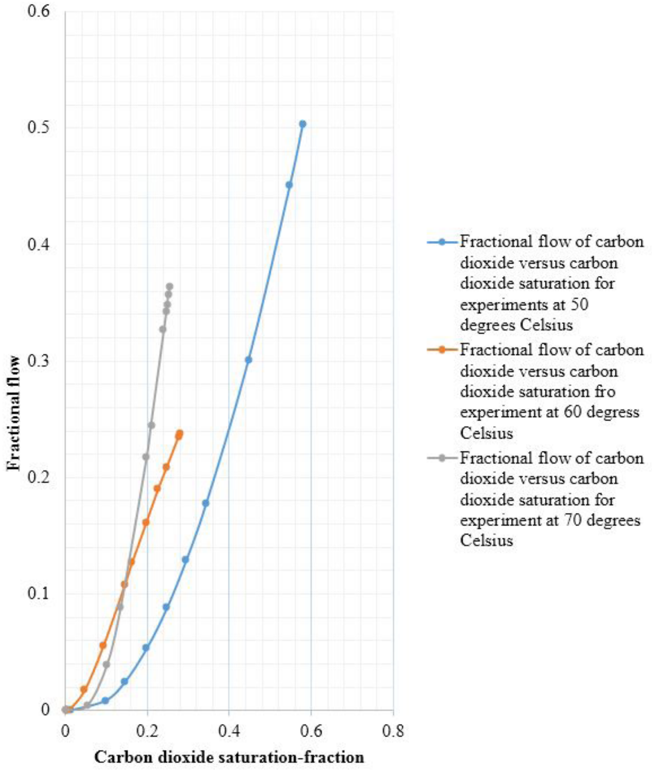

Figure 11: Fractional flow of carbon dioxide versus carbon dioxide saturation for experiments at different temperatures.

Per our hypothesis that at 323 K higher concentration of hydrogen ions will be produced, one would expect higher relative mobility of brine and lower relative mobility of injected carbon dioxide. This is seen from values of end point relative permeability of carbon dioxide at 323 K (Table 4). It is lowest at this temperature. One would also expect that the specific shock velocity of carbon dioxide at 323 K will be the lowest. (Figure 12) shows a plot of carbon dioxide fractional flow curve with Welge tangents. The velocity of the specific shock, which is the velocity of the front, is calculated using information about fractional flow at the point where the tangent drawn from the lowest injection fluid saturation touches the fractional flow curve. Equation (24) was used for this computation. Accordingly, computed values are 0.11 for experiment at 323 K, 0.50 for experiment at 333 K and 0.13 for experiment at 343 K. From these results, the velocity of the front was lowest at 323 K due to the lower relative mobility of carbon dioxide at this temperature. At 333 K, the frontal velocity of the flood must be higher than that expected at 323 K.

This is exactly the case. However, at 343 K, a much higher relative mobility is expected but, this was the opposite. The reason for this can be ascertained by considering the effect of temperature on gas dynamic viscosity. Generally, the dynamic viscosity of a gas increases with temperature due to increase momentum diffusivity [52, 53]. Table 4 shows that carbon dioxide has the highest dynamic viscosity at 343 K. At 343 K, there is high resistance to flow coupled with less carbon dioxide solubility. This condition causes greater water wettability and the lowest specific shock velocity for carbon dioxide.

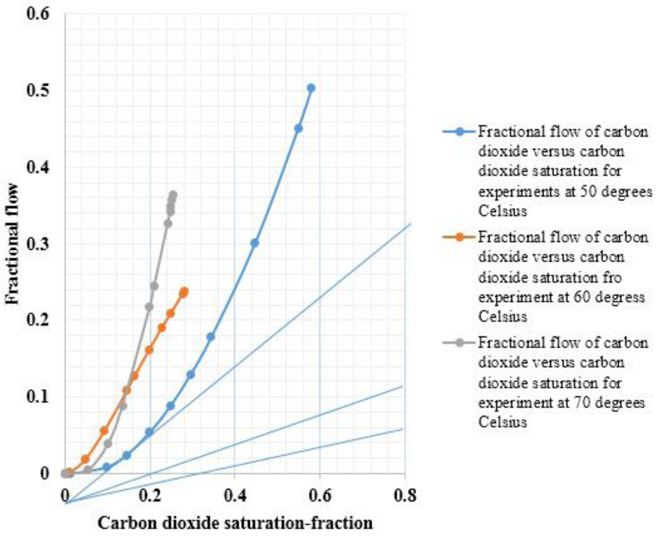

Figure 12: Fractional flow curves for carbon dioxide with at different temperatures with Welge tangents specific shocks.

Coupling (Figure 2) with the temperature dependent depth based on the temperature dependent dissociation constant of carbonic acid, the most optimum depth for geological sequestration is 1600 meters. However, depths corresponding to 10 degrees less or above 323 K are also suitable since injected carbon dioxide can still be under supercritical conditions to warrant optimization of available pore space for more storage. This is because at supercritical conditions, carbon dioxide has liquid-like densities [54] while maintain its gaseous nature by virtue of having dynamic viscosities similar to those of gases.

Conclusion

Geological storage of anthropogenic carbon dioxide in deep saline aquifers for reducing global carbon emission is technically and economically feasible due to advances in deep well drilling technology. However, in view of the projected daily increase of carbon dioxide emission from power plants and other emission sources due to the projected growth in global energy consumption, seeking efficient geological carbon storage is necessary to be able to geologically sequester large volumes of carbon dioxide. The task of efficiently injecting anthropogenic carbon dioxide into deep saline aquifers requires subsurface storage conditions to be understood in relationship to the physics of the two-phase flow of carbon dioxide in saline aquifers. Most importantly, the water-rock interaction deserves to be understood. Generally, water-rock interactions reduce water wetting of rock minerals making it possible to displace it for efficient storage. This means the geological conditions under which the water-rock interaction will result in optimum geological storage must be thoroughly understood. In this paper, we have reviewed literature to understand the temperature dependence of the dissociation constant of carbonic acid, which produces hydrogen ions for the water rock interaction. We have also reviewed literature to understand intermolecular theory related to interfacial tension. Based on these two understandings, we have proposed hypotheses and these hypotheses have been tested experimentally. The following sum up our conclusion:

- The production of Hydrogen ions, which are responsible for increasing solid-liquid interfacial tension will be maximum at 323 K, meaning that the greatest reduction of solid-liquid interfacial tension will occur at 323 K, by Young's equation.
- The relative mobility of brine will be maximized at all saturations at 323 K.
- The relative permeability of brine will be maximized at all saturations at 323 K.
- The most optimum temperature condition for carbon dioxide storage in saline aquifers is 323 K.
- According to our experimental results, the irreducible water saturation at 323 K was the least followed by that at 333 K, with the irreducible water saturation at 343 K being the highest.
- Our experimental results also show that the relative permeability of carbon dioxide at irreducible water saturation was highest at 323 K. This reflects the generally lower relative mobility of this phase at 323 K, which was the reason behind efficient water displacement and lower irreducible water saturation at this temperature.
- Based on a mean global geothermal gradient of 25 ^{o}C per kilometer, the most optimum depth for geological storage is 1600 meters.

Acknowledgements

The authors are grateful to the Department of Process Engineering and Applied Science, Dalhousie University who made their petroleum research lab available for the tests performed in this study. We are also indebted to the Office of Research, Teaching and Graduate Studies, Cape Breton University for their financial support.

References

1. Lackner KS (2002) Carbonate chemistry for sequestering fossil carbon. Annual review of energy and the environment 27: 193-232.
2. Holloway S (2001) Storage of fossil fuel-derived carbon dioxide beneath the surface of the earth. Annual Review of Energy and the Environment 26: 145-166.

3. Svensson RO, Odenberger M, Johnsson F, Strömberg L (2004) Transportation systems for CO_2-application to carbon capture and storage. Energy conversion and management 45: 2343-2353.

4. Goldberg DS, Takahashi T, Slagle AL (2008) Carbon dioxide sequestration in deep-sea basalt. Proceedings of the National Academy of Sciences 105: 9920-9925.

5. Xu X, Chen S, Zhang D (2006) Convective stability analysis of the long-term storage of carbon dioxide in deep saline aquifers. Advances in water resources 29: 397-407.

6. Eccles JK, Pratson LN, Newell RG, Jackson RB (2009) Physical and economic potential of geological CO2 storage in saline aquifers. Environ. Sci. Technol 43: 1962-1969.

7. Bake R (1998) Reservoir Management for Waterfloods-Part II. January 37: 12-17.

8. Espinoza DN, Santamarina JC, (2010) Water-CO2-mineral systems: Interfacial tension, contact angle, and Diffusion-Implications to CO2 geological storage. Water resources research 46.

9. Kim YW, Kneafsey TJ, Tokunaga TK, (2012) Dewetting of silica surfaces upon reactions with supercritical CO2 and brine: pore-scale studies in micromodels. Environmental science & technology 46: 4228-4235.

10. Drummond S (1981) Boiling and Mixing of Hydrothermal Fluids: Chemical Effects on Mineral Precipitation. Pennsylvania State University Ph.D. thesis.

11. Giammar DE, Bruant RG, Peters CA, Giammar DE, Bruant RG, et al. (2005) Forsterite dissolution and magnesite precipitation at conditions relevant for deep saline aquifer storage and sequestration of carbon dioxide. Chemical Geology 217: 257-276.

12. Bruant RG, Celia MA, Guswa AJ, Peters CA (2002) Safe Storage of CO2 in Deep Saline Aquifers. The authoritative voice of the environmental research community 36: 240-245.

13. Rosenbauer RJ, Koksalan T, Palandri JL (2005) Experimental investigation of CO_2-brine-rock interactions at elevated temperature and pressure: implications for CO_2 sequestration in deep-saline aquifers. Fuel processing technology 86: 1581-1597.

14. Plummer LN, Busenberg E (1982) The solubilities of calcite, aragonite and vaterite in CO_2-H_2O solutions between 0 and 90 C, and an evaluation of the aqueous model for the system $CaCO_3$-CO_2-H_2O. Geochimica et cosmochimica acta 46: 1011-1040.

15. Øren PE, Pinczewski WV (1995) Fluid distribution and pore-scale displacement mechanisms in drainage dominated three-phase flow. In Multiphase Flow in Porous Media. Springer Netherlands 105-133.

16. Amott E (1959) Observations relating to the wettability of porous rock. Published in Petroleum Transactions, AIME 216: 156-162.

17. Kwok DY, Neumann AW (1999) Contact angle measurement and contact angle interpretation. Advances in colloid and interface science 81: 167-249.

18. Chow TS (1998) Wetting of rough surfaces. Journal of Physics: Condensed Matter 10: 445.

19. Tombácz E, Libor Z, Illes E, Majzik A, Klumpp E, (2004) The role of reactive surface sites and complexation by humic acids in the interaction of clay mineral and iron oxide particles. Organic Geochemistry 35: 257-267.

20. Elmofty SE, Shokir EE (2003) Effect of surface active agents on electrokinetic and wettability changes of reservoir rocks. Emirates Journal for Engineering Research 8: 35-40.

21. Sverjensky DA (1994) Zero-point-of-charge prediction from crystal chemistry and solvation theory. Geochimica et Cosmochimica Acta 58: 3123-3129.

22. Fowkes FM (1962) Determination of interfacial tensions, contact angles, and dispersion forces in surfaces by assuming additivity of intermolecular interactions in surfaces. The Journal of Physical Chemistry 66: 382-382.

23. Boehm HP (1971) Acidic and basic properties of hydroxylated metal oxide surfaces. Discussions of the Faraday Society 52: 264-275.

24. Oss CJ, Good RJ, Chaudhury MK (1988) Additive and nonadditive surface tension components and the interpretation of contact angles. Langmuir 4: 884-891.

25. Pardo Q, Portoles S (1995) Students' and teachers' misapplication of Le Chatelier's principle: Implications for the teaching of chemical equilibrium. Journal of Research in Science teaching 32: 939-957.

26. Quílez-Pardo J, Solaz-Portolés, JJ (1995) Students' and teachers' misapplication of Le Chatelier's principle: Implications for the teaching of chemical equilibrium. Journal of Research in Science teaching 32: 939-957.

27. Sposito G (1981) The operational definition of the zero point of charge in soils. Soil Science Society of America Journal 45: 292-297.

28. Chatelier RC, Drummond CJ, Chan DY, Vasic ZR, Gengenbach TR, et al. (1995) Theory of contact angles and the free energy of formation of ionizable surfaces: application to heptylamine radio-frequency plasma-deposited films. Langmuir 11: 4122-4128.

29. Jung JW, Wan J (2012) Supercritical CO2 and ionic strength effects on wettability of silica surfaces: Equilibrium contact angle measurements. Energy & Fuels 26: 6053-6059.

30. Broseta D, Tonnet N, Shah V (2012) Are rocks still water-wet in the presence of dense CO2 or H2S? Geofluids 12: 280-294.

31. Smith CR, Tracy GW, Farrar RL (1992) Applied reservoir engineering. Oil & Gas Consultants Intl.

32. Hui MH, Blunt MJ (2000) Effects of wettability on three-phase flow in porous media. The Journal of Physical Chemistry, B 104: 3833-3845.

33. Anderson WG (1987) Wettability literature survey part 5: the effects of wettability on relative permeability. Journal of Petroleum Technology 39: 1-453.

34. Tang GQ, Firoozabadi A (2000) Relative permeability modification in gas-liquid systems through wettability alteration to intermediate gas-wetting. In SPE Annual Technical Conference and Exhibition (S. 1-15). Society of Petroleum Engineers.

35. Dardaganian SG (1958) The Application of the Buckley-Leverett Frontal Advance Theory to Petroleum Recovery. Journal of petroleum technology 10: 49-52.

36. Pope GA (1980) The application of fractional flow theory to enhanced oil recovery. Society of Petroleum Engineers Journal 20: 191-205.

37. Welge HJ, Johnson EF, Ewing SP, Brinkman FH (1960) The linear displacement of oil from porous media by enriched gas. Journal of Petroleum Technology 13: 787-796.

38. Huang WT (1962) Petrology. McGraw-Hill Book Company.

39. Barker CE, Pawlewicz MJ (1986) The correlation of vitrinite reflectance with maximum temperature in humid organic matter. In Paleogeothermics 79-93.

40. Anovitz LM, Cole DR (2015) Characterization and Analysis of Analysis of Porosity and Pore Structures. Reviews in Mineralogy and Geochemistry 80: 61-164.

41. Bennion B, Bachu S (2005) Relative permeability characteristics for supercritical CO2 displacing water in a variety of potential sequestration zones. In SPE Annual Technical Conference and Exhibition (S. 1-15). Society of Petroleum Engineers.

42. Bennion B, Bachu S, (2005) Relative Permeability Characteristics for Supercritical CO2 Displacing Water in a Variety of Potential Sequestration Zones in the Western Canada Sedimentary Basin. SPE Annual Technical Conference and Exhibition, 9-12 October (S. 1-15). Dallas, Texas: SPE.

43. Noh M, Lake LW, Bryant SL, Araque-Martinez A (2004) Implications of coupling fractional flow and geochemistry for CO2 injection in aquifers. In SPE/DOE Symposium on Improved Oil Recovery. Society of Petroleum Engineers (S. 11). Society of Petroleum Engineers.

44. Bourgoyne A, Millheim K, Chenevert M, Young F, (1984) Applied Drilling Engineering-SPE Textbook Series Volume 2. Society of Petroleum Engineers (SPE).

45. Robert J, Chillingarian G, Kumar S (1989) Surface Operations in Petroleum Production. Amsterdam: Elsevier Science.

46. Nordbotten JM, Celia MA, Bachu S (2005) Injection and storage of CO2 in deep saline aquifers: analytical solution for CO2 plume evolution during injection. Transport in Porous media 58: 339-360.

47. Institute GC (2012) Core Flooding Laboratory- Berea Injectivity Tests. Von https://hub.globalccsinstitute.com/publications/predicting-co2-injectivity-properties-application-ccs-sites/13-core-flooding-laboratory-berea-injectivity-tests abgerufen

48. Ennis-King J, Paterson L (2007) Coupling of geochemical reactions and convective mixing in the long-term geological storage of carbon dioxide. International Journal of Greenhouse Gas Control 1: 86-93.

49. Ennis-King J, Paterson L, Gale J, Kaya Y (2003) Rate of dissolution due to convective mixing in the underground storage of carbon dioxide. - 6th International Conference, Kyoto, Japan. Greenhouse Gas Control Technologies.

50. Li K, Shen P, Qing T (1994) A New Method for Calculating Oil-Water Relative Permeabilities with Consideration of Capillary Pressure. Mechanics and Practice 16: 46-52.

51. Duana Z, Sun R (2003) An improved model calculating CO2 solubility in pure water and aqueous NaCl solutions from 273 to 533 K and from 0 to 2000 bar. Chemical Geology 19: 257-271.

52. Beal C (1946) The Viscosity of Air, Water, Natural Gas, Crude Oil and Its Associated Gases at Oil Field Temperatures and Pressures. Society of Petroleum Engineers 165: 94-115.

53. Schäfer M, Richter M, Roland S (2015) Measurements of the viscosity of carbon dioxide at temperatures from (253.15 to 473.15) K with pressures up to 1.2 MPa. The Journal of Chemical Thermodynamics 89: 7-15.

54. Desimone JM, Tumas W (2003) Green Chemistry Using Liquid and Supercritical Carbon Dioxide. Oxford University Press.